Astro. Lett. and Communications, 1989, Vol. 27, pp. 321–331
Reprints available directly from the publisher
Photocopying permitted by license only
Printed in the United States of America

Simulated Observations of Low Energy Gamma Ray Sources

L. BASSANI, R. C. BUTLER, E. CAROLI, G. DI COCCO, L. NATALUCCI, A. SPIZZICHINO and J. B. STEPHEN *Istituto TE.S.R.E. (C.N.R.)*
Via de' Castagnoli, 1–40126 Bologna, Italy

(Received February 20, 1988)

A series of Monte Carlo simulated observations of γ-ray sources has been obtained for the Zebra telescope, using recent observational data. The results of the simulations are analyzed in order to assess both the sensitivity and imaging capability of the instrument during a typical balloon flight.

It is shown that sources like the Crab Nebula, the Quasar 3C273 and the Seyfert galaxy NGC4151 will be observable over the entire energy range of the instrument (0.2–10 MeV) at the few tens of sigma confidence level and will be located with an accuracy of the order of a few arc minutes. Furthermore, the simulations furnish an estimate of the capability of the telescope to resolve complex structured sources such as SS433 or crowded regions of the sky like that of the Galactic Center.

1. INTRODUCTION

The exploration of the low energy (0.2–10 MeV) γ-ray sky has lagged behind the investigations in other regions of the electromagnetic spectrum. The underlying reasons are related to the problems encountered in the instrument design and are associated with the detection of such penetrating photons.

For example, massive shielding was employed in the first generation of γ ray detectors in order to provide directionality by means of collimation. The result was a heavy telescope having a small collection area, poor angular resolution and no proper imaging capability. Furthermore, many of the pioneering observations in this energy range have been performed by means of balloon borne telescope systems and have therefore been limited to a small number of celestial targets.

Surprisingly, in spite of all these difficulties, a wide variety of object type have been positively identified as low energy γ ray emitters, indicating that much is to be learnt from a more comprehensive study of the sky at these wavelengths.

The results obtained so far have also indicated the requirements necessary for the next generation of γ ray telescopes: a factor of 10 improvement in sensitivity, a point source location ability to the order of few arcminutes and a wide energy range covering the few MeV region. An increase in sensitivity means that the number of detectable objects will increase accordingly. If for example a $\log N/\log S$ distribution of 3/2 is valid for the extra-galactic case, then we may expect that the number of visible sources will increase to about 150 for a 10 fold improvement in sensitivity (Bassani *et al.* 1984). Similarly, in the galactic case, it is expected that for a uniform disk population of sources ($\log N/\log S$ distribution of 1) a telescope with the same sensitivity will be able to detect about 50–60 sources (Coe *et al.* 1982).

On the other hand, the improved angular resolution made possible by recent technical developments, should lead to unambiguous identifications of γ-ray sources in some cases, and should facilitate the problem of finding optical counterparts in other cases. The introduction of the coded aperture mask technique will allow γ-ray images of the sky to be made, thus placing the γ-ray work on an equal footing with other branches of Astronomy (Caroli *et al.*, 1988). This technique, modulating the flux incident on a position sensitive detection plane is especially suitable for instruments designed to have large apertures or operating above 10 keV, where concentrating techniques are less effective or not applicable.

Finally the particular choice of the few MeV energy range depends on the belief that the emission at these wavelengths carries interesting information on the emitting regions themselves (i.e. spectral structures, nuclear lines, annihilation features and so on) (Bassani *et al.*, 1984, White, 1986).

The Zebra telescope has been designed to overcome the early instrumentation problems mentioned above and to meet the astrophysical requirements necessary to make progress in γ-ray Astronomy (Charalambous *et al.* 1984, Butler *et al.* 1986). Here, we present a series of Monte Carlo simulated observations of γ-ray sources employing the Zebra telescope in order to assess both the sensitivity and the imaging capability of the instrument during a typical balloon flight.

2. THE ZEBRA TELESCOPE

The configuration of the Zebra telescope consists of two identical and independent detection modules (total geometric area $\sim 5000\,\mathrm{cm}^2$) mounted at either side of a 3 axis gimbal system (Figure 1a).

Each module consists of:

a) a position sensitive (PS) detection plane made of an array of 9 NaI(Tl) scintillation crystals bars embedded in a U shaped set of 13 not position sensitive NaI(Tl) bars having the same dimensions of the PS bars (Figure 1b).
b) a coded aperture mask placed at a distance of 3.5 m in front of the PS detection plane (Figure 1c).

Each crystal bar of dimensions $55 \times 5.8 \times 5$ cm, is encapsulated in a thin aluminium housing and viewed at each end by a 2 inch photomultiplier (PM) tube. The position and energy of the interacting photons are computed by analysis of the amplitudes of the coincident PM tube signals (Butler *et al.* 1986).

The second layer of NaI(Tl) bars (non position sensitive) is used as an active anticoincidence system as is a plastic scintillator placed in front of the PS bar array. Detection plane bars immediately adjacent to the "event" bar are likewise used as veto counters. In this way it is possible to have a large sensitive area, which is actively shielded by inorganic scintillators which are themselves used, in turn, as detection elements.

Furthermore the Zebra design not only allows the instrument to achieve good active shielding and therefore high sensitivity ($\simeq 3 \cdot 10^{-4}\,\mathrm{ph/(cm^2\,sec)}$ at 1 MeV)

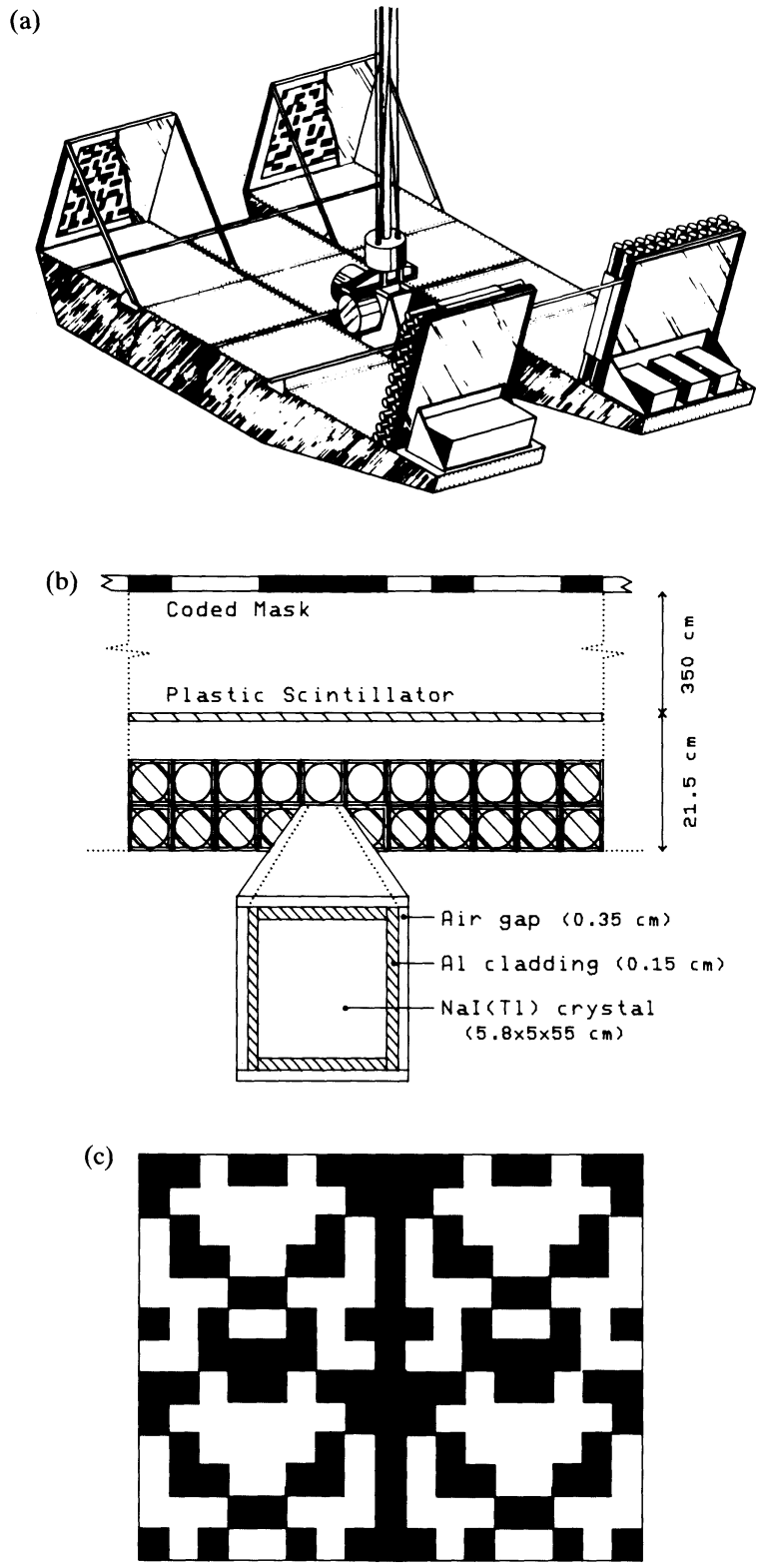

FIGURE 1 (a) An artist impression of the Zebra telescope. (b) Schematic view of one detection module, with a close-up view of one bar unit. Circles represent PM tubes. The shaded bars are employed for anticoincidence as is the plastic scintillator. (c) Complete pattern (13×17) of the coded mask employed.

by efficiently using all the material employed, but also provides it with imaging capability and therefore good angular resolution, by means of the coded aperture mask technique.

The mask (Figure 1c) is made of 2 cm thick tungsten alloy elements arranged in a 2×2 mosaic (minus one row and one column) of a 9×7 Hadamard basic pattern (Caroli *et al.*, 1987). The fully coded field of view is approximately 7×9 degrees within which the telescope has an intrinsic angular resolution better than 1° (FWHM) and a point source location of typically a few arc minutes (depending on the source signal to noise (S/N) ratio).

The telescope is currently undergoing the integration and testing phase and is scheduled to fly for the first time in Spring 1989 from the NASA Balloon Base at Palestine (Texas, USA). Due to current problems with stratospheric balloons only one detection plane will be employed for the first flight.

3. THE MONTE CARLO DESCRIPTION

A Monte Carlo simulation code designed to efficiently evaluate the response function of the Zebra telescope to observations of typical γ-ray sources has been written in Fortran *V* for implementation on a Cray. The details of the Monte Carlo can be found in Natalucci *et al.* (1986); here we briefly outline the main characteristics of the simulation code for clarity.

The Monte Carlo simulation is structured in such a way that a detection apparatus may be divided into a series of functionally independent subsystems, thus allowing the user to follow a stepwise simulation, where each step uses as input the output of the previous one. In our particular case, the Zebra subsystems are the mask, the detection unit and the electronics response. Once the input parameters are given (i.e. source intensity, spectral shape and location), the Monte Carlo simulates the interaction of a parallel beam of photons with the mask (step 1) and of the product of this first step with the detector (step 2).

The interaction processes taken into account are:

1) *Photoelectric absorption.* The incoming photon loses all its energy unless a *K*-fluorescence X-ray secondary photon is produced by de-excitation of the detector material. This effect is only considered for primary photon energies below a given threshold, where the escape probability of the secondary photon is not negligible, and the photon is assumed to be isotropically emitted.
2) *Compton scattering.* A scattering angle is selected from the Klein-Nishina differential cross section distribution, via a rejection sampling technique, while the azimuthal angle is randomly chosen, polarization being neglected. The secondary photon direction and energy are calculated along with the energy lost in the material.
3) *Pair production.* The positron is assumed to annihilate from rest with the creation of two 0.511 MeV photons isotropically emitted in opposite directions. The annihilation point is assumed to coincide with the interaction point, leading to a slight overestimate of peak events due to the omission of positron escape effect.

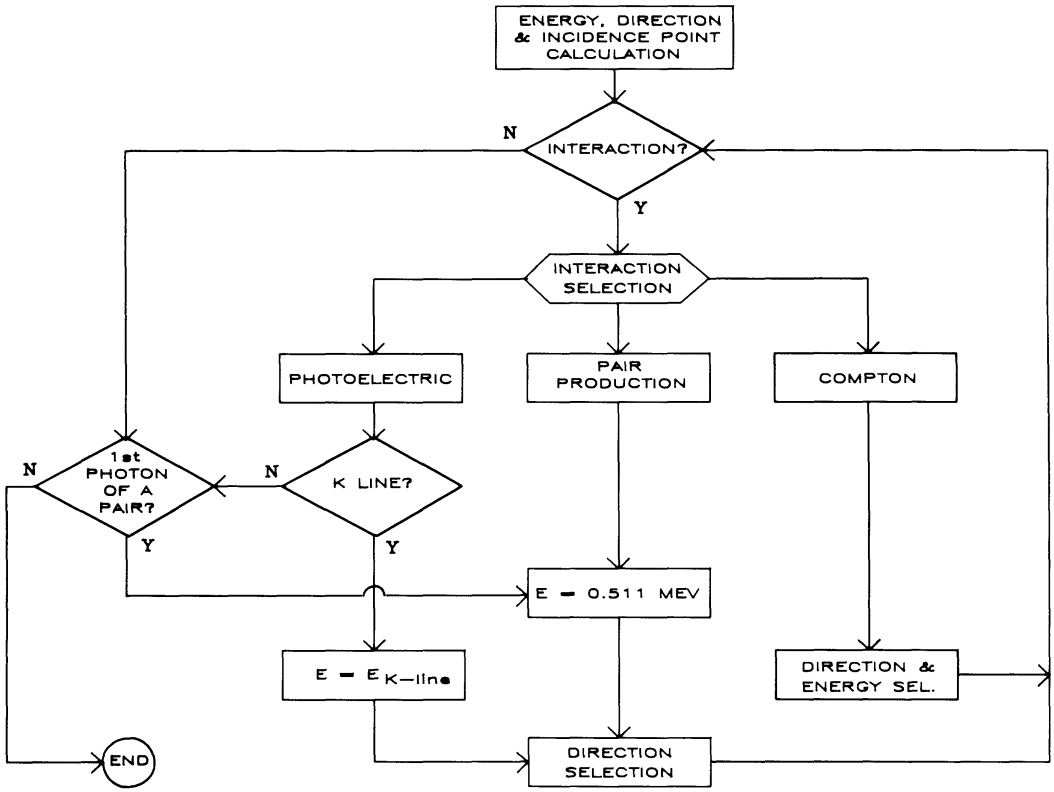

FIGURE 2 Flow-chart outlining the physical model adopted for the Monte Carlo simulation code.

The main processes which are neglected are bremsstrahlung and ionization losses derived from electron and positron recoiling or scattering.

The flow chart outlining the physical model adopted for the simulation code is shown in Figure 2. Starting from the photon history calculated in step 2, a pulse height analysis is performed by means of specific programs in which the signal generation and processing model of the detector under study is implemented. The complete electronics logic is also implemented in the program in order to fully estimate the performance of the anticoincidence system (i.e. the NaI(Tl) bars and the plastic scintillator veto counter).

The Monte Carlo code uses some experimental data as input parameters in order to evaluate the entire process of energy and position reconstruction. Therefore, by taking into account all the complexity of the Zebra system (mask, aluminium structure, bar structure, anticoincidence systems etc.) the simulation allows the user to obtain the counts spectrum of typical γ-ray targets and therefore to assess both the sensitivity and imaging capability of the telescope.

4. THE SIMULATED OBSERVATIONS

The Zebra telescope has been designed as a balloon borne telescope system and therefore its performance will be limited in terms of observational program and source observation time. Only the implementation of the same instrument on a

satellite or space borne platform will allow a full exploitation of the capabilities of the telescope by increasing the number of observations and their duration.

The short timescale of a balloon flight forces the flight program to be centered around a few individual observations of short duration. Furthermore, the first flight of the instrument dictates that the choice of the targets to be observed be limited to intense and well known sources both for calibration and scientific purposes.

With all these constraints in mind, we have carried out a number of simulations of likely targets, both of galactic and extragalactic nature. In particular we have simulated point-like sources (as the Crab Nebula, the Quasar 3C273 and the Seyfert Galaxy NGC4151), crowded regions of the sky such as the Galactic Center region and complex structured sources such as SS433.

The simulations were performed assuming a typical observation length of 2×10^4 sec and employing the whole Zebra detection area of $\sim 5000\,\mathrm{cm}^2$ (comprising two sets of 9 position sensitive bar scintillators).

In order to assess the effects of the background on the observational results, we have simulated both a uniform and a slowly varying background contribution of the same integrated intensity (calculated from Mandrou *et al.* (1977) as $11.04 \cdot E^{-1.65}$ counts/(cm^2 sec keV) and scaled to the Zebra configuration). In the case of uniform background, the counts are assigned to each detection plane pixel of size 0.4×6.5 cm following a gaussian distribution with mean and variance equal to the number of counts expected in the energy range considered. The form assumed for the non uniform background was a combination of a convex distribution along the bar with a concave distribution across each set of bars. The maximum percentage of non-uniformity with respect to the mean background value was chosen to be $\sim 10\%$. Recent calibration data indicate this to be the most likely form of instrumental background (Figure 3).

Once the background is added to the simulated data, a deconvolution based on a direct cross-correlation method is applied in order to reconstruct the sky image. The algorithm used correlates the simulated shadowgram with all the different

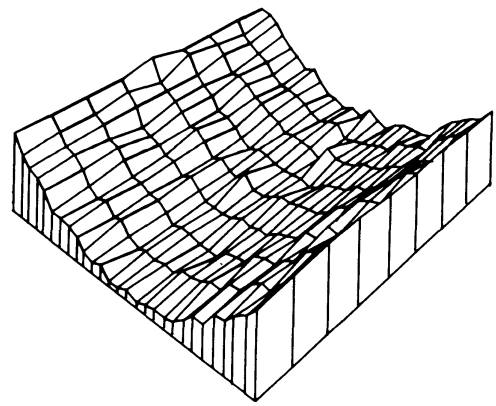

FIGURE 3 The shape of the non-uniform background assumed in the simulation is similar to the one observed experimentally during the calibration of the Zebra detection plane. The maximum variation from the mean is $\sim 10\%$.

TABLE I

Source name	Monte Carlo Spectrum*		Significance ($n\sigma$) by Energy Band					
			0.18–0.4	0.4–0.75	0.75–1.5	1.5–3.0	3.0–10.0	0.18–10.0
Crab Nebula	$23.8E^{-2.3}$	(1)	58.9	23.4	8.4	4.8	3.6	47.4
3C 273†	$0.014E^{-1.2}$ $109.0E^{-2.6}$	(2) (3)	29.1	29.9	18.0	10.0	1.9	44.3
NGC 4151	$1.6\ 10^{-5}e^{-E/2120}$	(4)	14.4	17.0	18.3	14.6	19.2	19.1
			0.18–0.4	0.47–0.56	0.56–3.0	1.5–10		0.18–10.0
GC-A1743-322	$6.80E^{-2.39}$	(5)	18.6	3.1	6.3	1.1		13.4
GC-GX3 + 1	$2.35E^{-2.39}$	(5)	8.4	29.4	2.5	2.9		9.2
GC-511 keV	$0.65\ 10^{-3}$	(6)						
GC-1742–294	$0.98E^{-1.88}$	(5)	18.2	5.2	8.3	3.2		13.5
					1.1–1.3	1.4–1.6		0.18–1.7
SS433 1.2 MeV	$1.1\ 10^{-3}$	(7)			11.4	8.5		4.5
SS433 1.5 MeV	$1.5\ 10^{-3}$	(7)						

* Flux in photons/($cm^2\ s^1\ keV^1$) for the continuum and ph/($cm^2\ s^1$) for the line emission.

† 3C 273. Double power law with a break at 0.6 MeV assumed.

Ref. (1) Schonfelder (1983); (2) Bignami *et al.* (1981); (3) Bezler *et al.* (1984); (4) Perotti *et al.* (1979); (5) Knight *et al.* (1985); (6) Riegler *et al.* (1981); (7) Lamb *et al.* (1983).

possible matrices which have the same dimension of the basic pattern and are each a subset of the mask matrix where the opaque and transparent elements are weighted in a suitable way (in the Zebra case by −1 and +1). The particular choice of a Hadamard basic pattern guarantees an exact reconstruction and minimizes the variance of the statistical errors (Caroli *et al.* 1984). The sources simulated are listed in Table I together with the expected significance relative to various energy channels.

As a first result, the simulation furnishes an estimate of the capability of the telescope to detect a point source of the same intensity of the Crab Nebula, NGC4151, 3C273 or a fraction of one. Because of the finite spatial resolution of the detector, not all source counts are ascribed to the source after the deconvolution process is applied. This effect is energy dependent and becomes more evident going from high to low energies.

Figure 4 represents the detection shadowgram and a 3D projection of the deconvolved image of the Crab Nebula after the addition of the original Monte Carlo data of a uniform background. As the non-uniform background employed is slowly varying across the position sensitive detector it is possible to remove or at least substantially reduce it by suitable filtering in frequency space (i.e. removing low frequency Fourier components). Figure 5 shows the image of NGC4151 before and after this treatment.

It is evident from the figures and Table I that all simulated point source observations have good statistical significance over the whole energy range of the instrument (few tens of sigma confidence level) as well as in the individual energy channels. The error in the calculated significance is estimated to be less than 1% on the basis of the values obtained and the total number of events detected. As a second result, the simulations of SS433 and the Galactic Center region are able to assess the imaging capability of the instrument. In the energy range considered here, a rigorously correct imaging simulation of these sky regions is difficult to

(a)

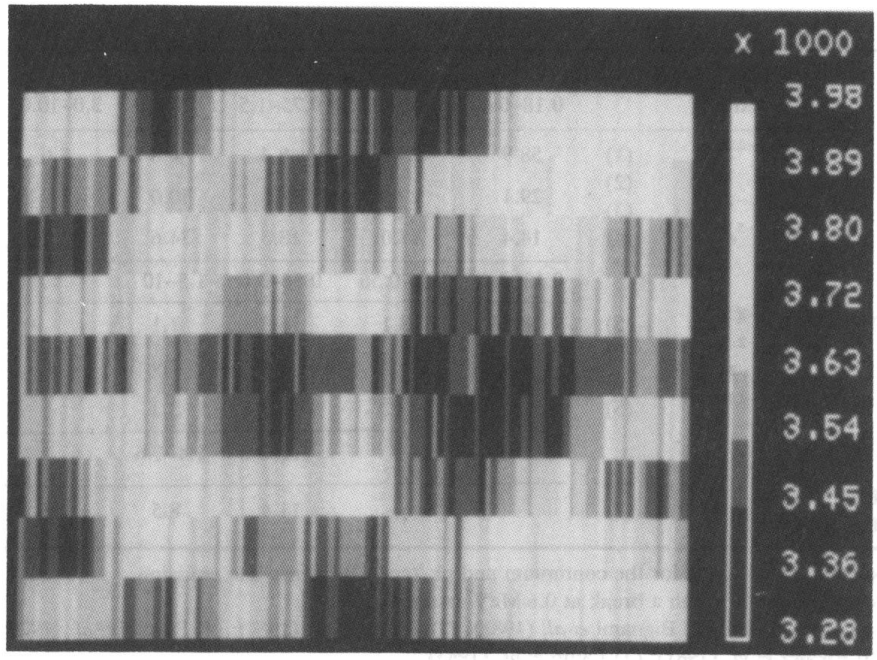

(b)

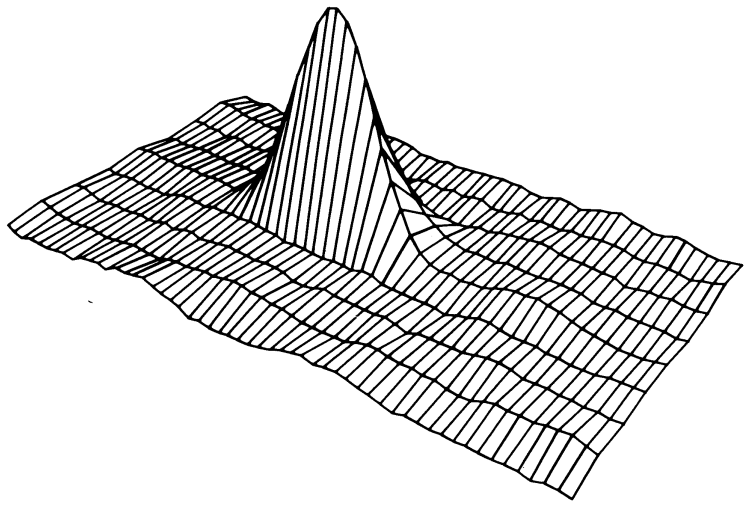

FIGURE 4 (a) Shadowgram of the Crab Nebula on one detection module relative to the whole Zebra energy range (0.2–10 MeV). The shadow of one complete 7×9 cycle of the mask can be seen, the blurring being due to the finite PSD resolution and to transparency of the opaque mask elements. The scale on the side refers to the number of counts on one detector pixel scaled to the area of one mask pixel. (b) 3-D projection of the deconvolved image of the Crab Nebula (0.2–10 MeV). See color plate XIII.

(a)

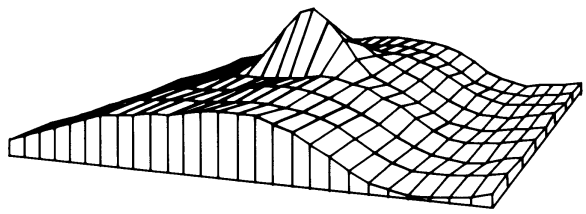

FIGURE 5 Examples of 3D projection of deconvolved images of point-sources superimposed on the non-uniform background shown in Figure 3; (a) without filtering, (b) with filtering using a high pass filter.

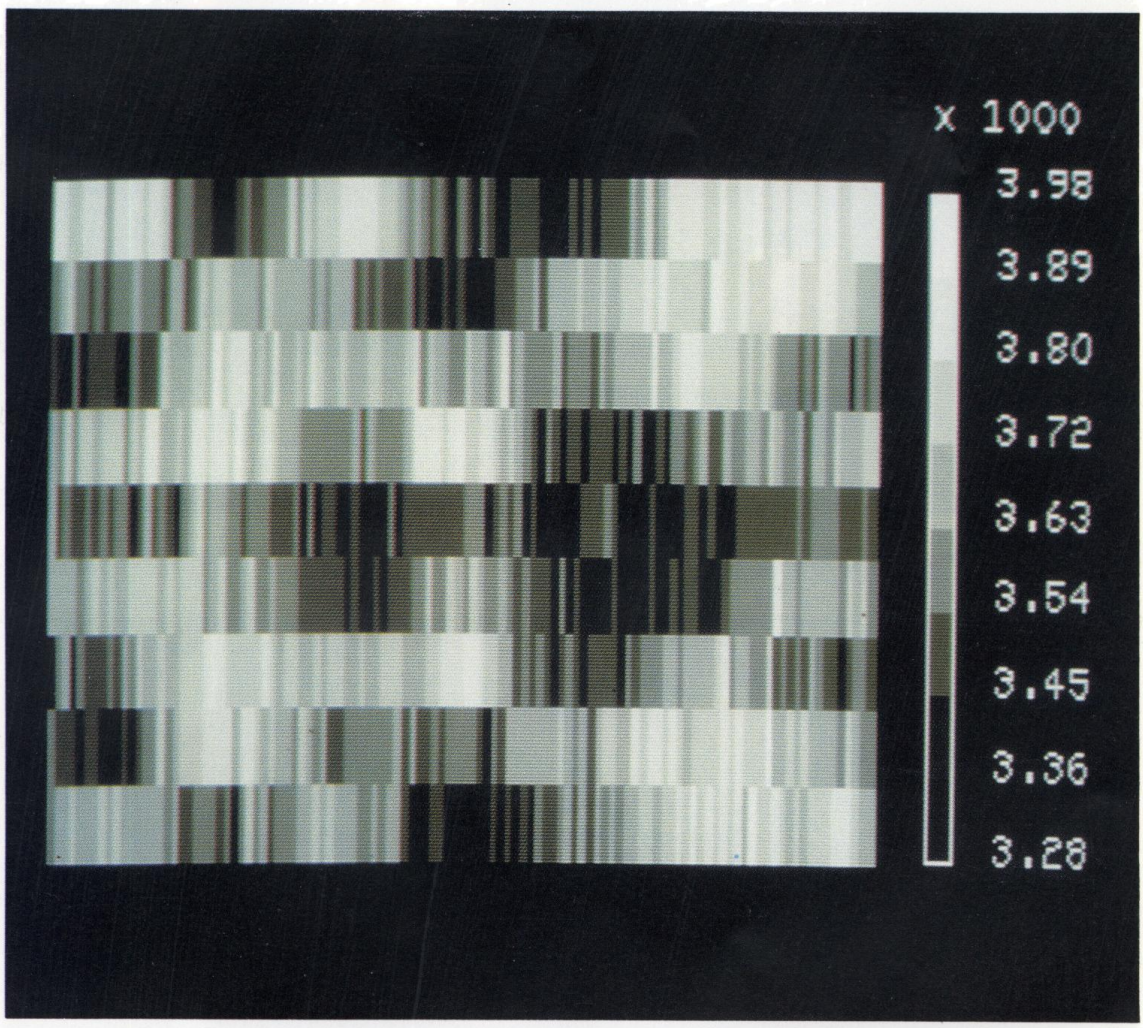

ASTROPHYSICAL LETTERS AND COMMUNICATIONS
COLOR PLATE XIII. See L. Bassani *et al.*, Figure 4, page 328.

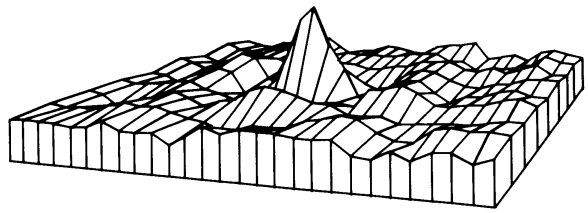

FIGURE 5 (*cont'd*)

(a)

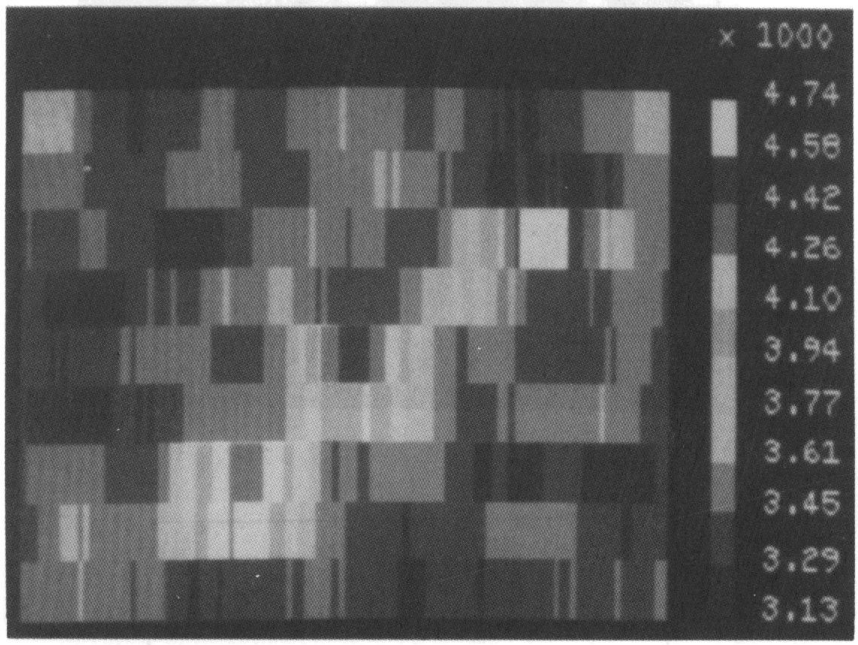

(b)

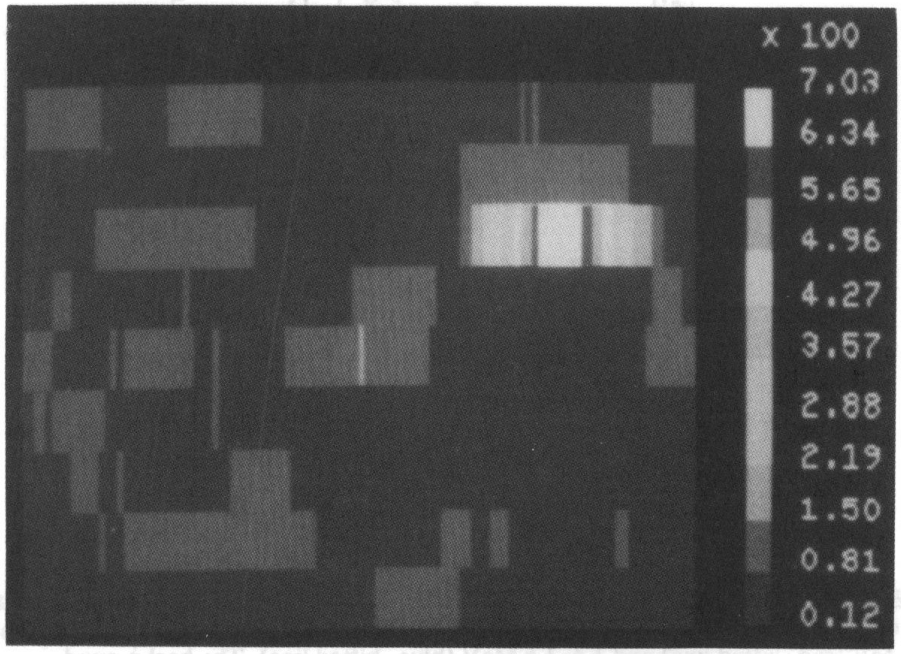

FIGURE 6 (a) Images of the Galactic Center region (from l. to r. A 1743–322, A 1742–294 and GX 3 + 1) over the entire Zebra energy range, and (b) at the annihilation line energy (0.47–0.56 MeV). See color plate XIV.

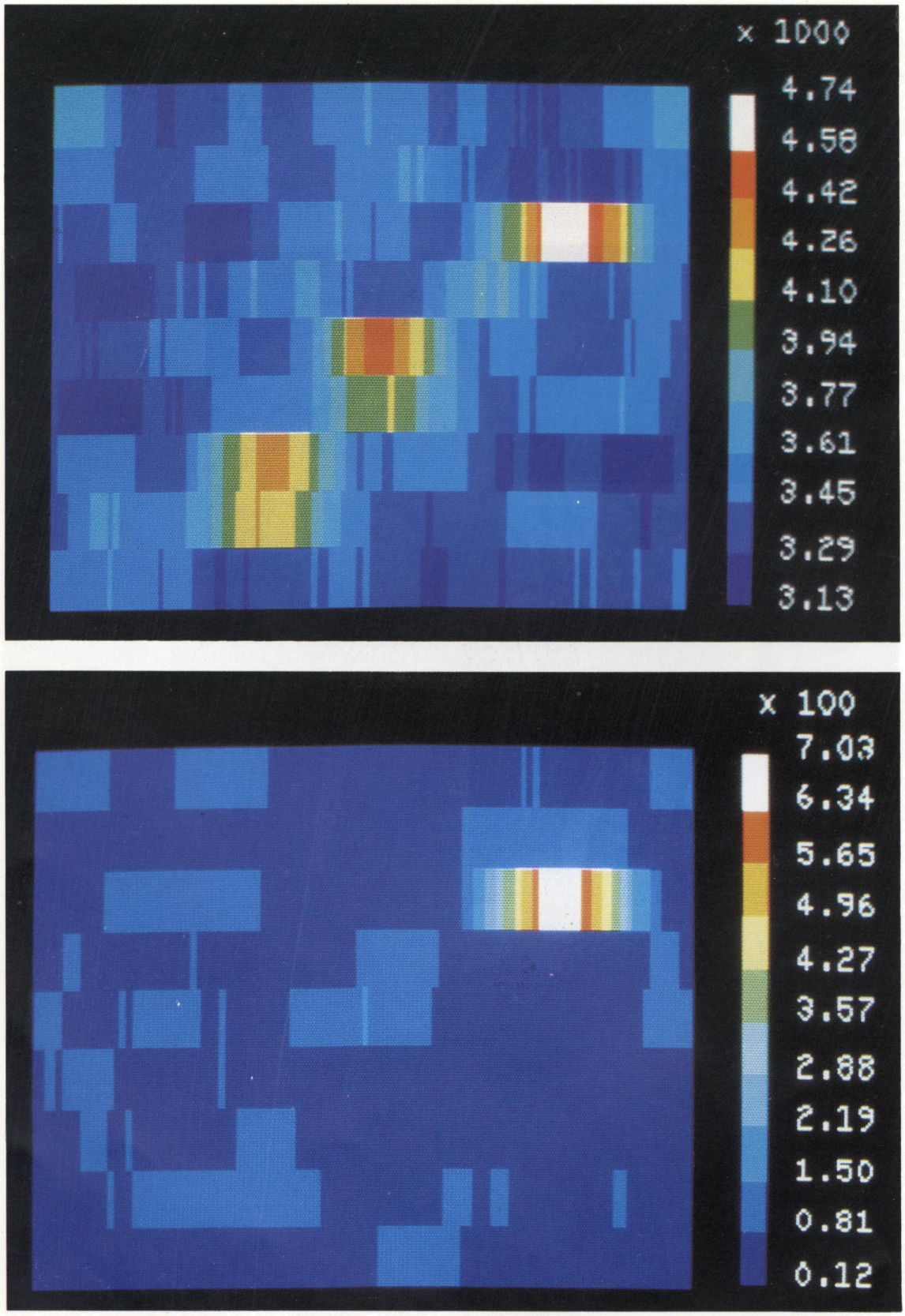

ASTROPHYSICAL LETTERS AND COMMUNICATIONS
COLOR PLATE XIV. See L. Bassani *et al.*, Figure 6, page 329.

(a)

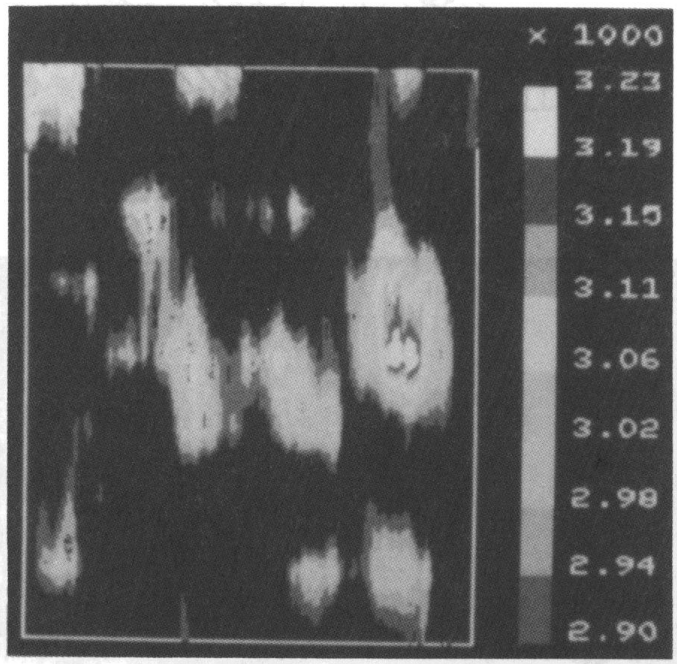

(b)

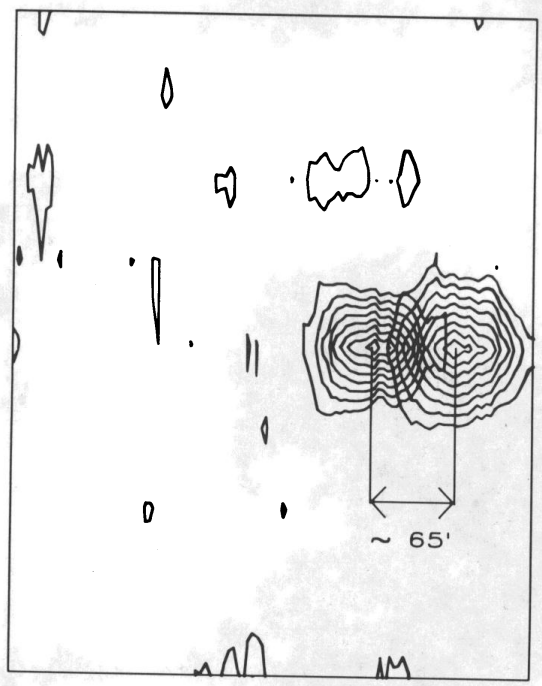

FIGURE 7 (a) The deconvolved image of SS433 in the 1.1 ÷ 1.6 MeV Region (redshifted and blueshifted Mg^{24} line). (b) Overlapping of the SS433 images obtained in the two energy ranges 1.1–1.3 MeV (red shifted line) and 1.4–1.6 MeV (blue shifted line). The background threshold in each picture is different for enhancing the peak characteristics. See color plate XV.

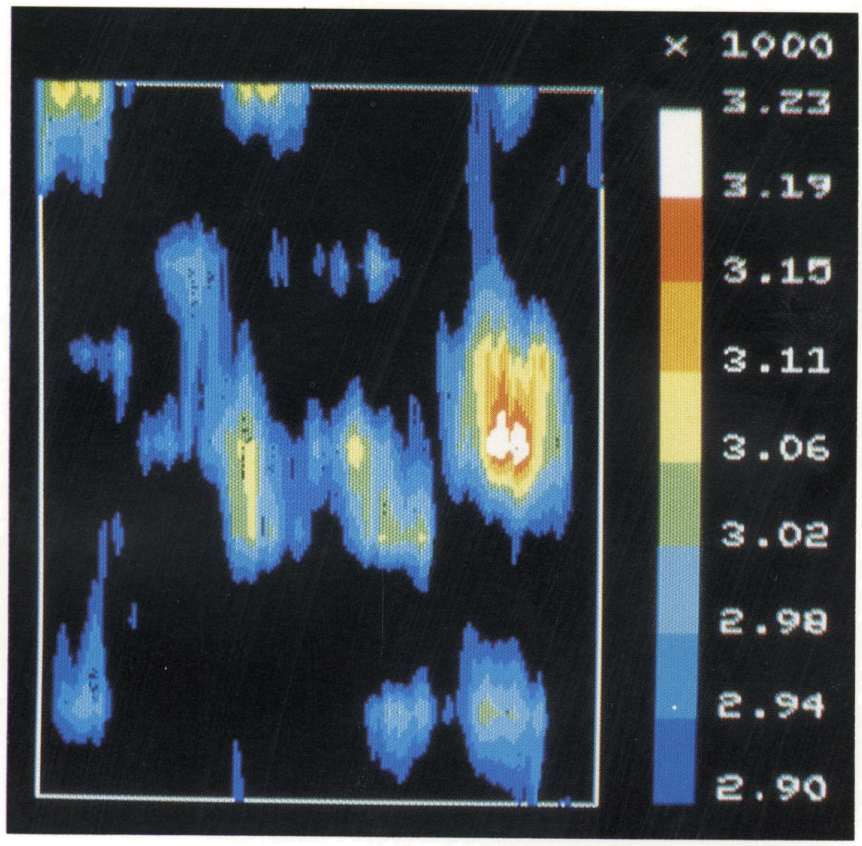

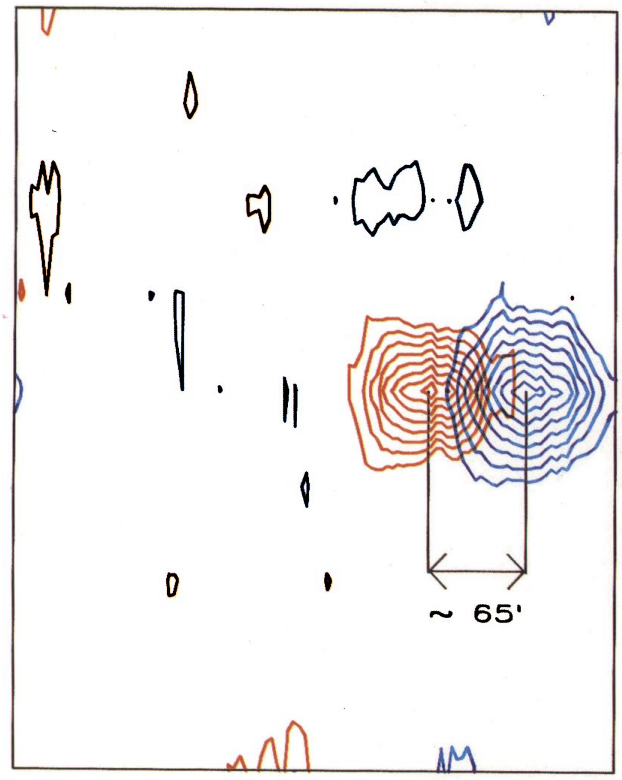

ASTROPHYSICAL LETTERS AND COMMUNICATIONS
COLOR PLATE XV. See L. Bassani *et al.*, Figure 7, page 330.

achieve given the paucity of currently available observational data. However, the construction of the exact sky image is not necessary since the purpose of the simulation is to evaluate qualitatively the ability to resolve complex and crowded regions. This justifies for example our simplified picture of the galactic center region where, following the results of Knight *et al.* (1985), only 3 sources associated with localized celestial objects are considered. The other two sources listed in Knight *et al.* (1985) are at the border of our field of view and, in addition, too weak to be detectable by Zebra in a 2×10^4 sec observation. We have also considered the presence of the 511 keV annihilation feature (Riegler *et al.*, 1981) and assumed it to be point-like and coincident with one source.

In the case of the Galactic Center region, all the 3 sources simulated appear at a few σ confidence level up to about 1 MeV. Moreover the good separation obtained between the central source (presumed to be the Galactic Center source itself) and the two lateral ones is evident in the false colour image of this sky region (Figure 6) and gives another estimate of the imaging quality of Zebra. This instrument will allow the Galactic Center region to be resolved at γ-ray energies down to angular distances of about 1° degree (150 pc) and perhaps even less for a longer observation time and more sophisticated analysis methods. Therefore Zebra should be able to localize the 511 keV annihilation line feature within the galactic center region with a point source location accuracy of the order of 2–3 arcminutes.

As for SS433, we have adopted the kinematic model proposed by Lamb *et al.* (1983), which consists of two components, one blue and one redshifted, of the 1.369 MeV line from a nuclear transition of ^{24}Mg, separated by 67′ and oppositely ejected by the central source. It is evident from Figure 7 that the resolving power of the Zebra telescope will allow a complete spatial separation of the two line features once the data relative to the two energy channels of interest here are fully analyzed. The angular separation obtained between the source peaks in the two images is in excellent agreement with the model (~5′).

REFERENCES

Bassani, L. *et al.* (1984), Active Galactic Nuclei, Dyson J. E. ed., Manchester University Press, 252.
Bignami, G. F. *et al.* (1981), *Astr. Ap.* **93,** 71.
Bezler, M. *et al.* (1984), *Astr. Ap.* **136,** 351.
Butler, R. C. *et al.* (1986), Proc. of the 15th I.S.T.S. Symposium, H. Matsuo Ed. in Chief, AGNE Publ. Inc., Vol. II, 1859.
Caroli, E. *et al.* (1984), *Nuovo Cimento* **7,** 786.
Caroli, E. *et al.* (1987), *Space Sci. Rev.*, **47,** 349.
Charalambous, P. M. *et al.* (1984), *Nucl. Instr. Meth.* **221,** 183.
Coe, M. J. *et al.* (1982), *Mon. Not. R. Astr. Soc.* **200,** 385.
Knight, F. K. *et al.* (1985), *Ap. J.* **290,** 557.
Lamb, R. C. *et al.* (1983), *Nature* **305,** 37.
Mandrou, P., Niel, M., and Vedrenne, G. (1977), Recent Advances in Gamma Ray Astronomy, ESA SP 124, 59.
Natalucci, L. *et al.* (1986), Proc. of the 2nd European Simulation Congress, Antwerp (Belgium) 484.
Perotti, F. *et al.* (1979), *Nature* **282,** 484.
Riegler, G. R. *et al.* (1981), *Ap. J.* **248,** L13.
Schönfelder, V. (1983), *Adv. Spa. Res.* **3,** N4, 59.
White, S. R. (1986), UCR/IGPP 86/19 Internal Report.